ROYAL SOCIETY OF CHEMISTRY

PAPER

Check for updates

Thermodynamic study of CsCaCl₃ using neutron diffraction†

Craig L. Bull, [ID] *ab Christopher J. Ridley, [ID] a Nicholas P. Funnell, [ID] a Sumit Konar [ID] ‡b and James Cumby [ID] b

The pressure and temperature phase diagram of the halide-based perovskite, CsCaCl₃ is investigated using neutron diffraction. At ambient pressure, it undergoes a cubic to tetragonal phase transition at approximately 95 K. The structural evolution is characterised by changes in Cs and Ca coordination, bond lengths, and polyhedral volumes. Heat capacity measurements reveal a discontinuity at the phase transition, where we use a two-term Debye model to show the presence of two distinct contributions. Under pressure, CsCaCl₃ exhibits phase transitions from cubic to tetragonal to rhombohedral symmetry, which can be understood when comparing the relative compressibilites of the $CaCl_6$ and $CsCl_n$ (where $n = 12$ for the cubic and 8 for the tetragonal and rhombohedral phases). Overall, this study provides experimentally derived thermodynamic properties and a tentative phase diagram of CsCaCl₃ as a function of pressure and temperature.

1 Introduction

The aristotype perovskite structure is cubic (space group $Pm\bar{3}m$) with corner shared BX_6 octahedra surrounding a AX_{12} polyhedron (see Fig. 1). Of particular interest to this manuscript is the case where X represents a halide (F, Cl, Br, I), rather than oxygen. Fernández *et al.*[1] previously demonstrated that materials with the general formula $ABCl_3$ crystallise in this perovskite structure, with a tolerance factor between 0.81 and 0.9.[2,3] Halide-based perovskites, as with the oxide analogues, often demonstrate temperature and pressure-driven polymorphism, with crystallographic symmetry deviating from or converging towards the cubic aristotype *via* octahedral rotation/distortion, or A-site cation displacement. For example, cubic $CsSrCl_3$ transforms to tetragonal then orthorhombic then monoclinic symmetry at 385 K, 375 K and 362 K respectively.[1,4] $CsPbCl_3$ is also highly polymorphic, with multiple phase transitions over a very narrow temperature range.[5] The application of hydrostatic pressure as a tuning parameter is an efficient way of generating materials with new crystalline structures with intrinsic physical properties.[6] Pressure tends to increase the electron density therefore enhancing the repulsive forces within a material,

often resulting in unexpected behaviour. The halide based perovskites are good analogues for perovskite oxides under high-pressure conditions, with the advantage of showing greater compressibilities compared to their oxide counterparts.[7]
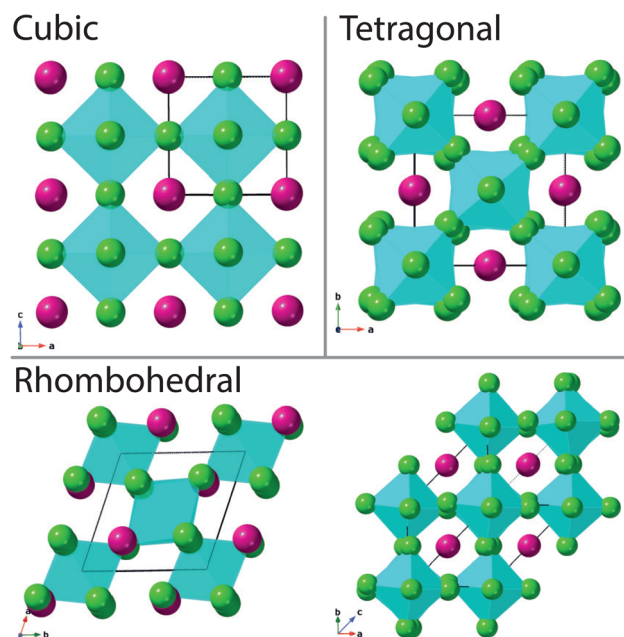

Fig. 1 Crystal structure of cubic aristotype perovskite, ABX_3, and the tetragonally and rhombohedrally distorted variants. In all three structures the A-site atoms are shown in purple, the X-site atoms are green and the B-site atoms are within the green BX_6 octahedra. The solid black lines outline the crystallographic unit-cell in each structure.

a ISIS Neutron and Muon Source, Rutherford Appleton Laboratory, Didcot, Oxon, OX11 7XN, UK. E-mail: craig.bull@stfc.ac.uk

b School of Chemistry, University of Edinburgh, David Brewster Road, Edinburgh EH9 3FJ, Scotland, UK

† Electronic supplementary information (ESI) available. See DOI: https://doi.org/10.1039/d4tc00592a

‡ Present address: Joseph Banks Laboratories, School of Chemistry, University of Lincoln, Lincoln LN6 7DL, UK.

4800 | *J. Mater. Chem. C*, 2024, **12**, 4800–4808

This journal is © The Royal Society of Chemistry 2024

For example, the pressure driven isostructural phase transition of $CsPbCl_3$ at room temperature.[8]

At 293 K, $CsCaCl_3$ is cubic and has been shown to transform to tetragonal symmetry upon cooling below 95 K.[9] It is an effective scintillator material, and its doped derivatives find applications in fields such as medical imaging and high-energy physics experiments.[10–12] More generally, inorganic chloride perovskites also find applications in light-emitting diodes, photodetectors and field effect transistors.[13–16] Understanding the structural and thermodynamic/physical property relationships of such materials is key to the design of novel materials with tailored physical properties which can prepared by chemical tuning. The application of pressure allows a clean and rapid determination of structure–property relationships which provides information for materials design suitable for devices with specific physical properties. In this study we have used neutron diffraction to study the structure of $CsCaCl_3$ as a function of temperature and pressure. Isothermal compression of $CsCaCl_3$ at 290 and 190 K reveals two structural phase transitions allowing the determination of a tentative phase diagram.

2 Experimental

2.1 Sample synthesis and characterisation

Calcium chloride (anhydrous, $\geq 93.0\%$) and caesium chloride (99.999%) were dried under dynamic vacuum in fused silica tubes at 473 K overnight, and were transferred immediately to a glovebox where an equimolar proportion of each were mixed thoroughly in an agate mortar. The mixture was subsequently inserted into another fused quartz tube, sealed and removed from the glovebox where the tube was encapsulated by flame sealing under vacuum. The sealed quartz tube was placed upright inside a box furnace and annealed at 1273 K for 12 hours, prior to cooling to ambient conditions. The quartz tube was returned to the glovebox for storage. Heat capacity measurements were performed on a 6.5 mg lump of $CsCaCl_3$, taken from the melted sample before grinding the remaining sample into a fine powder for the diffraction measurements. The isobaric heat capacity, c_p, was measured using a PPMS (Quantum Design Inc.) using the relaxation method over the temperature range 4–300 K, on heating. The isochoric heat capacity, c_v, was calculated using the expression: $c_v = c_p - T\alpha_v^2 B_0 V_m$. Where α_v is the volumetric thermal expansion coefficient, B_0 is the bulk modulus (assumed temperature independent), and V_m is the molar volume.

2.2 Neutron powder diffraction

All neutron-diffraction measurements were performed on the time-of-flight PEARL diffractometer.[17] The ambient pressure data were collected from the sample as-synthesised, loaded and sealed into a 6 mm diameter vanadium canister within a glovebox. The sealed can was loaded into a 50 mm diameter (Abingdon Scientific) vanadium tailed cryostat and then cooled to 5 K. Diffraction patterns were collected step-wise upon

warming. For the high-pressure measurements, the sample was loaded in a glove-box into an encapsulated TiZr gasket with a pellet of Pb as a pressure-marker[18] and perdeuterated methanol : ethanol (4 : 1 by volume) as a pressure-transmitting medium.[19] The gasket was sealed between two single-toroidal anvils, machined from zirconia toughened alumina, within a V3 Paris–Edinburgh press.[20] Diffraction patterns were obtained in the transverse scattering geometry in approximately 5 tonne steps up to a maximum of 60 tonnes applied load, collected for ~ 2 hours per step. The data were focused and corrected for attenuation using Mantid.[21] The crystallographic structures were Rietveld-refined against the resulting diffraction patterns using GSAS.[22] Fits to the unit-cell data and subsequent determination of equations-of-state were determined using PASCal.[23]
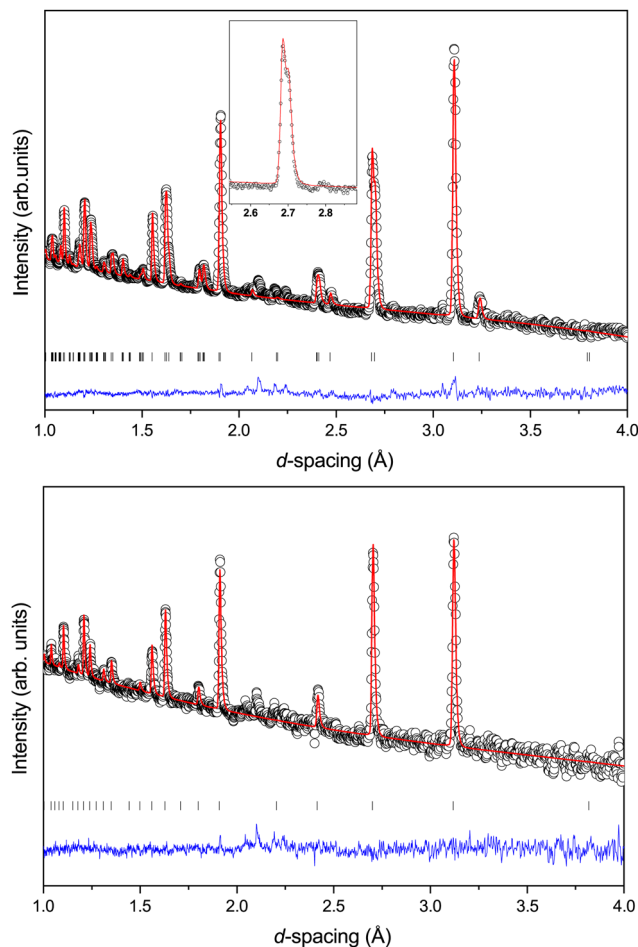
3 Results & discussion

3.1 Ambient pressure behaviour

Fig. 2 shows the neutron powder diffraction patterns at 260.0(1) and 5.0(1) K. Upon cooling below ~ 95 K a new reflection appears at ~ 3.24 Å, which can be indexed as the $\frac{3}{2} \cdot \frac{1}{2} \cdot \frac{1}{2}$ super-lattice reflection of the pseudo-cubic cell (corresponding to the R-point of the Brillouin zone). The R-point reflection is also accompanied by a splitting of the cubic 400 reflection at ~ 2.69 Å which index as the 220 and 004 reflections in the new tetragonal cell (space group $I4/mcm$, $a^0a^0c^+$ tilt system[24]). Our data collections are coarse in temperature steps however, we estimate that the transition from the cubic to tetragonal phase occurs at ~ 95 K which is in good agreement with previous experimental results.[9] Fig. 3 shows the thermal evolution of the pseudo-cubic lattice parameters for the cubic $(a = a_{pc})$ and tetragonal $(a_{pc} = a_{tet}/\sqrt{2}, c_{pc} = c_{tet}/2)$ phases.

In the tetragonal phase the Cs coordination reduces from 12 to 8 (with an associated point group change from $m\bar{3}m$ to $\bar{4}2m$), the $CaCl_6$ polyhedra remain unchanged in coordination number, but there is a change in point group symmetry from $m\bar{3}m$ to $4/m$. In both the cubic and tetragonal phases the derived structural parameters (polyhedral volumes and bond lengths) can be obtained following the parameterisation of Knight et al.,[25] a full tabulation of which is provided in the ESI.† These are derived from the lattice parameter (a) in the cubic phase, and the (a, c) lattice parameters, and the order parameter (ϕ) in the tetragonal phase. ϕ is the rotation of the $CaCl_6$ octahedra about [001]. This can be derived from the atomic coordinate of the Cl atom, u (where $\tan(\phi) = 4u$).[26] The refined structural parameters are given in Table 1 for the two data sets shown in Fig. 2, see the ESI,† for further temperatures.

The temperature evolution of the tetragonal lattice parameters have been fitted to a model related to an Einstein internal energy function;[27] the fits are shown as solid lines in Fig. 3. The fit function, and resulting fit parameters are provided in the ESI.† The symmetry-adapted tetragonal strain (detailed in the ESI,† and ref. 25), e_{tz}, tends towards 0 upon approaching the phase transition, as the cubic phase is by
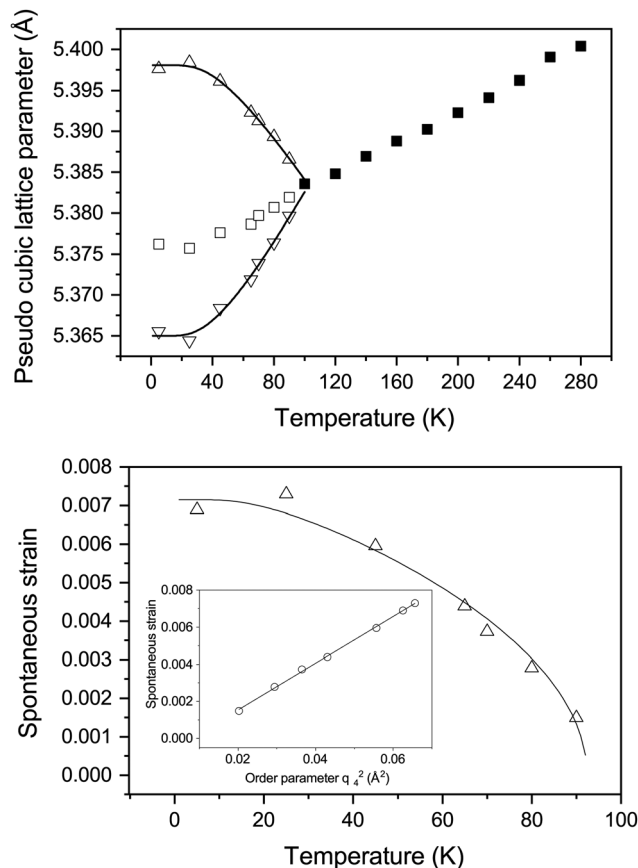
This journal is © The Royal Society of Chemistry 2024

J. Mater. Chem. C, 2024, 12, 4800–4808 | 4801

Fig. 2 Ambient pressure neutron diffraction patterns of CsCaCl$_3$. Top: Diffraction pattern and associated Rietveld refinement of CsCaCl$_3$ at 5.0(1) K, the inset shows an enlarged region around the split pseudo–cubic 400 reflection (220 and 004 reflections in the tetragonal phase). Bottom: Diffraction pattern and associated Rietveld refinement of cubic CsCaCl$_3$ at 260.0(1) K. In both panels the raw data are shown as open circles, the Rietveld fit to the data as a solid red line, the residual of fit is shown as a blue trace, and the vertical lines show the expected positions of Bragg reflections of the fitted phases. In both patterns there are contaminant vanadium peaks from the vanadium canister, $\sim$2.08 Å.

Fig. 3 Top: Variation in lattice parameter for CsCaCl$_3$ with temperature. Cubic lattice parameter for cubic phase as filled square symbols and the pseudo cubic lattice parameters for the tetragonal phase as unfilled triangles (a_{pc}) and c_{pc} as unfilled down triangles as defined in the main text. The derived a_0 from the tetragonal unit-cell volume is shown as unfilled squares. Bottom: Temperature variation of spontaneous strain e_{tz} (open triangle) as defined in the text. The inset shows the variation the spontaneous strain (e_{tz}) with the square of the order parameter ($q_4 \equiv \phi$). The solid lines show the fits to the data as described in the main text.

necessity free of tetragonal-strain. Following the work of Knight et al.,[25] it is possible to model the temperature dependence of e_{tz} with the following equation:

$$e_{tz} = a\theta_s \left[\left(\tanh\left(\frac{\theta_s}{\theta_c}\right) \right)^{-1} - \left(\tanh\left(\frac{\theta_s}{T}\right) \right)^{-1} \right]^m \quad (1)$$

where θ_s is the saturation temperature, θ_c the critical transition temperature and m the order parameter. We find a critical temperature of 92.4(4) K, $\theta_s = 28.8(6)$ K and the best fit obtained with the order parameter fixed at 0.5 and is shown in Fig. 3. The requirement for the crystal to be stress free under equilibrium conditions leads to the strain component (e_{tz}) taking the form:

$$e_{tz} = \frac{-4\lambda_2 q_4^2}{(C_{11}^0 + C_{12}^0)} \quad (2)$$

Table 1 Details of the Rietveld refined crystallographic models of CsCaCl$_3$ at 5.0(1) and 260.0(1) K at ambient pressure. A full list, for all temperatures measured, can be found in the ESI. For the cubic structure the space-group is $Pm\bar{3}m$; Wyckoff positions: Cs 1b, Ca 1a, Cl 3d. For the tetragonal structure the space-group is $I4/mcm$, Cs 4b, Ca 4c, Cl(1) 4a, Cl(2) 8h $\frac{1}{4} + u$, $\frac{3}{4} + u$, 0

Parameter	5.0(1) K	260.0(1) K
Symmetry	Tetragonal	Cubic
Space group	$I4/mcm$	$Pm\bar{3}m$
a (Å)	7.5880(3)	5.3991(3)
b (Å)	7.5880(3)	5.3991(3)
c (Å)	10.7953(5)	5.3991(3)
Unit-cell volume (Å^3)	621.57(7)	157.38(3)
Cl(2) u	0.0233	—
wR_p, R_p (%)	1.3, 1.5	1.46, 1.68
χ^2	1.02	0.6

where λ_2 is a coupling constant, and C_{ij}^0 are bare elastic constants.[25] The strain varies as the square of the order parameter ($q_4 \equiv \phi$) as shown in Fig. 3. The order parameter and

4802 | J. Mater. Chem. C, 2024, 12, 4800–4808

This journal is © The Royal Society of Chemistry 2024

measured lattice parameters are used to predict the behaviour of the bond lengths, polyhedral volumes and octahedral rotations with temperature in the tetragonal phase (see Fig. 4); overall the structural evolution is well described by the parameterisation.

The two distinct Ca–Cl bonds both decrease in length with increasing temperature, while in the cubic phase the single bond-length increases linearly as the temperature is increased, see Fig. 4. This is mirrored in the temperature dependence of the $CaCl_6$ polyhedral volume. This behaviour is analogous to that seen in the structurally-similar system $RbCaF_3$.[26] In the tetragonal phase the axial Cs–Cl(1) bond shows only a small variation with temperature, which is in contrast to the shorter bonded Cs–Cl(2) bond which rapidly increases in length with increasing temperature and this behaviour is mirrored by the longer non-bonding Cs–Cl(2) bond which reduces in length. In the cubic phase these three distinct bonds become equivalent and increase in length with increasing temperature. Overall, this results in a non-linear increase in the $CsCl_8$ polyhedral volume with temperature, becoming a linear increase for the

$CsCl_{12}$ polyhedra in the cubic phase. The octahedral tilting (ϕ) is also shown, tending to zero as the phase transition to the cubic phase is approached.

3.2 Heat capacity at ambient pressure

The temperature dependence of the unit-cell volume $V(T)$ can be fitted to a model based on statistical mechanics with the underlying Grüneisen approximation to the ambient pressure equation of state:[28] $V(T) = V_0 + (\gamma/B(T))U(T)$, where γ is the Grüneisen parameter, $B(T)$ is the bulk modulus, $U(T)$ is the internal energy function of the crystal, and V_0 is the unit cell volume at $T = 0$. As the full temperature dependence of $B(T)$ is unknown, it is hereby assumed to be temperature invariant i.e. $B(T) \approx B_0$, where B_0 is the isothermal bulk modulus. The internal energy can be approximated using a Debye model, the parameters for which can be fitted simultaneously against the volumetric and isochoric heat-capacity data (see ESI,† for details). Such a technique has been used extensively in the literature, for example in the study of $BaZrO_3$.[29] The isochoric heat capacity was calculated from the isobaric heat capacity as described in the experimental details, with the number of volume data-points limiting the overall fit. The full isobaric heat capacity dataset is available in the ESI,† and shows a clear discontinuity at the point of the transition to tetragonal symmetry between 90 and 100 K, as expected.

The heat capacity and volumetric data were fitted in this way in the tetragonal phase, where the bulk modulus has been assumed to be temperature invariant, fixed at the value determined at ambient temperature for the tetragonal phase (see Table 3). It was found that a single-term Debye model fitted the volumetric data well (giving $\theta_D = 267(8)$ K), but it could not account for the measured temperature dependence in the heat capacity, see Fig. 5. Instead, a two-term Debye model was used, representing separated cation and anion behaviour, significantly improving the fit. Despite the limited number of data points, the fits converged stably; the determined thermodynamic parameters from these fits are summarised in Table 2. The weighted average value for the Debye temperature is $\theta_{wD} = 304$ K, which is higher than that predicted recently from *ab initio* methods (233.7 K,[30] 225.67 K[31]). However both of these studies assumed cubic symmetry for the material, which may explain the discrepancy.

3.3 High pressure behaviour at 290 K

With increasing pressure, at 2.4(1) GPa a new broad but weak feature is observed at ∼3.1 Å in the diffraction pattern. This feature is in the same region as the *R*-point reflection observed upon cooling at 90 K and can be indexed accordingly. However, there are no other new reflections observed or splitting, within the instrumental resolution limits, suggesting that there is no measurable strain in the material. However, as shown in Fig. 6, at 4.2(1) GPa the reflection significantly sharpens and increases in intensity and is accompanied by a splitting of the pseudo-cubic 200 reflection and no observed splitting of the 111 reflection. This suggests that this phase has tetragonal symmetry and can
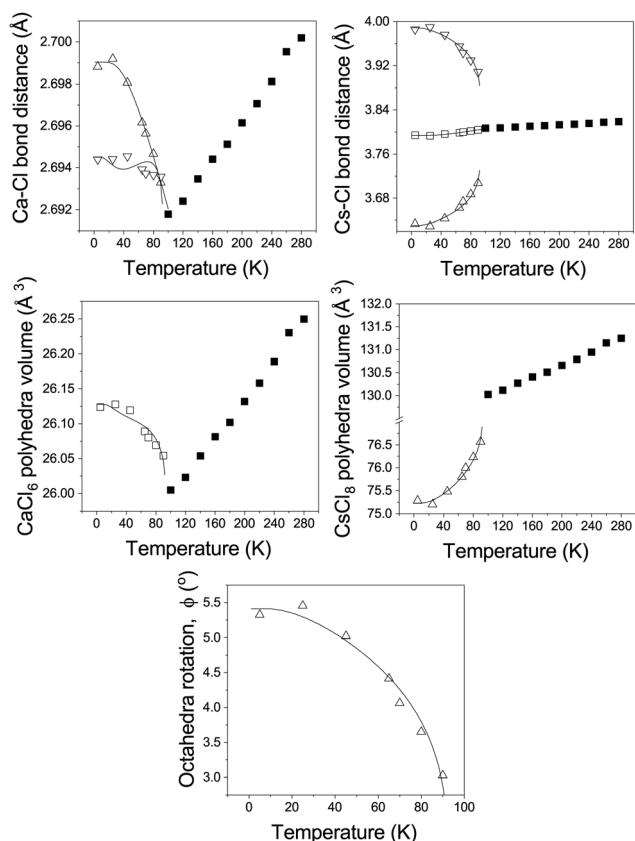

Fig. 4 Variation of bonds with temperature in $CsCaCl_3$. Top left: Ca–Cl bonds within the $CaCl_6$ octahedra. Top right: Variation of Cs–Cl bonds in the $CsCl_n$ polyhedra. Middle left: Variation of $CaCl_6$ octahedra volume. Middle right: Variation in $CsCl_n$ polyhedra volume. Bottom: Variation in octahedra tilt with temperature in the tetragonal phase. In all panels the open symbols are from the tetragonal phase and the solid symbols the cubic phase. The solid lines in the tetragonal phase region show the extrapolated behaviour from the variation in unit cell and q_4 as described in the main text.

Fig. 6   Changes in diffraction pattern of CsCaCl$_3$ with increasing pressure across the phase transition region. In the bottom trace the reflections from the cubic (c) phase are identified and those from lead identified by an asterisk. Upon increasing pressure the R point reflection from the tetragonal (t) phase appears (211t) and other reflections are split. At higher pressure the splitting which occurs from the rhombohedral (tr) phase is observed.
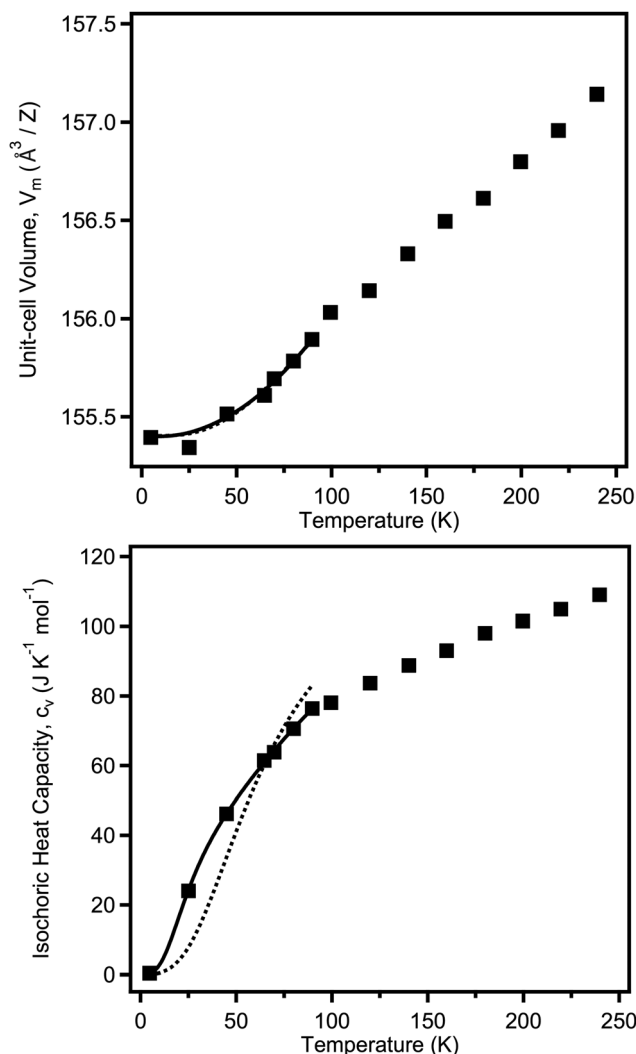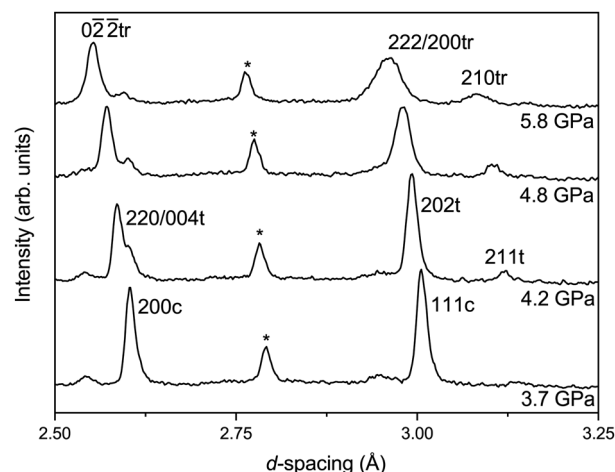
Fig. 5   Top: Unit-cell volume variation with temperature, as determined from neutron powder diffraction measurements at ambient pressure. Bottom: Isochoric heat capacity variation with temperature at ambient pressure. The markers represent the interpolated heat capacity data to match the temperature points measured using neutron diffraction. In both figures, the solid line represents the fit to the two-term Debye model, as discussed in the main text, and the dashed line (obscured in volume figure) represents the fit to the single-term Debye model.

At the next pressure point measured (4.8(1) GPa), the relative intensity of the 220/004 reflections change and the pseudo-cubic 111 reflection is seen to broaden (suggesting a peak splitting§), indicative of a transition to lower symmetry due to further tilting of the CaCl$_6$ octahedral units. This is caused by the freezing of phonons at the R-point (anti-phase tilt) or M-point (in-phase tilt) in reciprocal space of the cubic $Pm\bar{3}m$ structure. We do not observe an M-point reflection in the data set at high-pressure, though if it is very weak it could be masked by the background of the pressure–cell. The high sensitivity of neutron diffraction to chlorine would therefore indicate that, if present, an M-point distortion must be extremely small. We proceed assuming only an R-point distortion is present.

The pattern can be fitted with a rhombohedral phase, space group $R\bar{3}c$ ($a^- a^- a^-$) for which only the R-point reflections are present, with a small fraction of the tetragonal phase coexisting. An attempt to fit the data against a lower-symmetry model, for example with orthorhombic $Imma$ ($a^- a^- c^0$) symmetry, did not yield a satisfactory fit to the data. The pattern remains mixed phase up to the maximum pressure measured of 6.4(1) GPa. Upon recovery to ambient conditions the R-point reflection is lost, as is the splitting of the pseudo-cubic reflections, showing full reversibility.

Fig. 7 shows the variation in the unit-cell volume with pressure in each of the three phases described above. Also shown are the derived Birch–Murnaghan equations of state (EoS) for each phase; the fitted EoS parameters are listed in Table 3. The value of B_0 for the cubic phase of 25.3(9) GPa is

§ This follows the assumption that the sample is still under hydrostatic pressure conditions, as evidenced by the fact that the other reflections in the pattern remain sharp, while the absolute pressure remains below the hydrostatic limit for methanol:ethanol (4:1 by volume).

Table 2   Refined fitting parameters for the temperature dependence of the unit cell volume and isochoric heat capacity of CsCaCl$_3$ in the tetragonal phase

Parameter	
V_0 (Å^3)	155.4(3)
γ_1	6(2)
θ_{D1} (K)	461(12)
γ_2	2.0(5)
θ_{D2} (K)	118(3)
Mixing parameter, z	0.543(14)

be indexed on the $I4/mcm$ space group, equivalent to the low-temperature phase discussed above.

4804 | *J. Mater. Chem. C*, 2024, **12**, 4800–4808
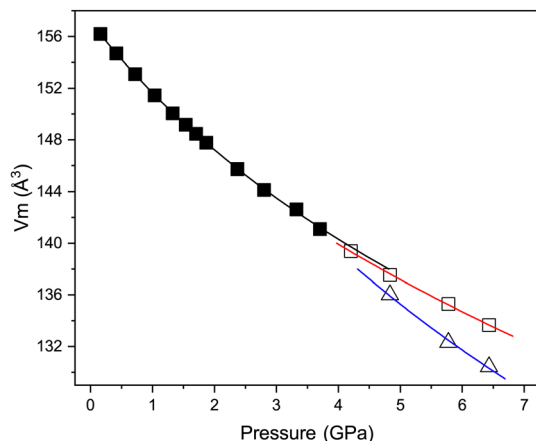
This journal is © The Royal Society of Chemistry 2024

Fig. 7 Variation in unit-cell volume per formula unit (V_m) with pressure of CsCaCl$_3$. The filled square for the cubic phase, unfilled red squares the tetragonal phase and the unfilled blue triangles the rhombohedral phase. The solid lines are the fitted Birch–Murnaghan EoS to the data points as described elsewhere. The number of formula units per unit cell (Z) of the cubic phase is 1, 4 for the tetragonal phase and 2 for the rhombohedral phase.

significantly lower than would be expected for oxygen-based inorganic perovskites for example CaTiO$_3$ the bulk modulus is 177 GPa,[32] and is not unexpected for halide based inorganic perovskites, for example, CsPbCl$_3$ has a B_0 of 45.6 GPa.[8] Theoretical prediction of B_0 for CsCaCl$_3$ suggest values between 23–32 dependent on the model used.[33,34] The value of B_0 is also comparable to polymeric halide compounds for example AuI which has a bulk modulus of 18 GPa.[35] The bulk modulus determined for the tetragonal phase is greater than that of the cubic phase, as would be expected from a denser phase. However, unusually, the higher-pressure rhombohedral phase has a lower bulk modulus than the cubic phase. The values of B_0 determined for the tetragonal and rhombohedral phases are unreliable (and only shown for completeness) as a result of the limited number of data points used for each fit. However, Fig. 7 clearly shows that the transition from cubic to tetragonal phase is close to second order in nature, given the almost continuous behaviour of the unit-cell volume across the phase-boundary and the first order like behaviour of the tetragonal to

rhombohedral phase where a clear discontinuity in unit-cell volume is observed in addition to phase co-existence.

For the determination of tetragonal strain (e_{tz}) in the tetragonal high pressure phase it is possible to use the equations described previously. However a_0, can be obtained by extrapolation of the cubic-phase EoS. Fig. 8 shows the variation in e_{tz} and a_{pc} with pressure for the tetragonal phase.

The structure of a rhombohedral symmetry perovskite with the $R\bar{3}c$ space group, has the atoms sited on Wyckoff positions: Cs 2a, Ca 2b, Cl 6e $\left(\frac{1}{4} - 2w, \frac{1}{4} + 2w, \frac{3}{4}\right)$. Here, w is the displacement of the Cl atom from the ideal cubic position and gives rise to tilting of the octahedra about the rhombohedral [111] axis. A value of $w = 0$ is the idealised cubic structure.[36] The magnitude of the octahedral tilt in the rhombohedral phase (ω) is given by $\tan \omega = 4\sqrt{3}e$.[37] In the rhombohedral phase, the error in lattice parameter determination makes meaningful interpretation of the strains difficult, and hence only the strain tensors e_{11}, e_{22} and e_{33} have been calculated. As described by Carpenter *et al.*[38] the definition is valid for the
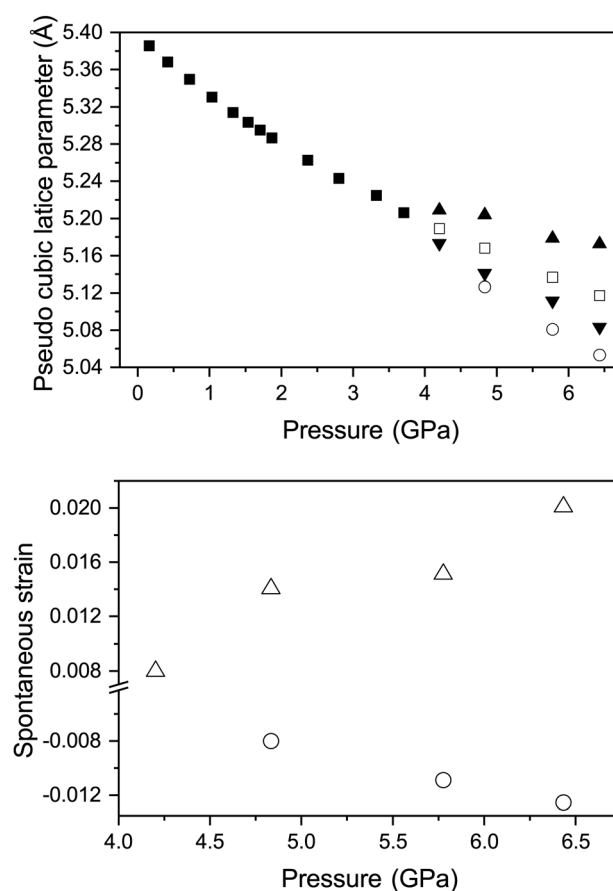

Table 3 Axial compressibilites and Birch–Murnaghan EoS values of the for all three phases of CsCaCl$_3$ with pressure at 290 K

Parameter	Cubic	Tetragonal[a]	Rhombohedral[a]
Axial compressibility			
a (TPa^{-1})	8.98(11)	6.5	9.3(2)
b (TPa^{-1})	—	6.5	8.5(4)
c (TPa^{-1})	—	3.9	8.4(2)
EoS order	3rd	2nd	2nd
V_0 (Å^3)	157.14(14)	617.1(19)	328.4(2)
B_0 (GPa)	25.3(9)	33.7(10)	17(2)
B'	5.9(6)	—	—

[a] The number of data points available significantly limits the validity of the values determined in the two high pressure phases, and are shown only for completeness.

Fig. 8 Top: Variation in reduced lattice parameters of CsCaCl$_3$ with increasing pressure. Cubic phase shown as filled squares, tetragonal phase as up and down filled triangles and the open circles are those of the rhombohedral phase. The unfilled squares are the extrapolated value for the cubic phase as determined from the EoS. Bottom: Variation in the spontaneous strain in the tetragonal (open triangles) and rhombohedral phase (open circles) of CsCaCl$_3$ with increasing pressure.

This journal is © The Royal Society of Chemistry 2024

J. Mater. Chem. C, 2024, **12**, 4800–4808 | **4805**

strain as the determined values of the pseudo-cubic cell angle $\left(\alpha_{pc} = 90 - \frac{\sqrt{3}}{2}(60 - \alpha_{rh})\right)$ is less then 90.5° and hence, can be defined as:

$$e_{11} = e_{22} = e_{33} = \frac{a_{pc}}{a_0} - 1 \qquad (3)$$

For the rhombohedral phase, the pseudo-cubic lattice parameter is defined as $a_{pc} = \frac{a_{rh}}{\sqrt{2}}$. The variation of a_{pc} and that of e_{11} with pressure is shown in Fig. 8. This shows that in both phases, the strains are deviating away from zero, and are becoming more strained/distorted with increasing pressure, however the magnitude of the strain is small.

Fig. 9 shows the variation in the Cs–Cl and Ca–Cl bond lengths in all three phases with increasing pressure. In the cubic phase both the Cs–Cl and Ca–Cl bond lengths are decreasing as per the decrease in unit-cell dimensions. In both the tetragonal and rhombohedral phase the Ca–Cl bonds are decreasing overall in length with increasing pressure. In the tetragonal phase it is clear that the octahedra are becoming more distorted as the two distinct Ca–Cl bonds deviate from each other in length with increasing pressure. The same behaviour is seen for the behaviour of the bonds forming the $CsCl_n$ polyhedra in both phases with increasing pressure. The variation of ω and ϕ for the rhombohedral and tetragonal phases respectively with increasing pressure at 290 K are also shown in Fig. 9. In both the tetragonal and rhombohedral phases the magnitude of octahedra tilt is increasing with increasing pressure. In the rhombohedral phase the octahedra are undistorted, however can homogeneously flatten or elongate along their triad axis of the octahedra and has been previously described by the factor ζ (the octahedral strain, defined following Megaw in the ESI†). The variation of ζ of the $CaCl_6$ octahedra for the rhombohedral phase is shown in Fig. 9 and shows that the octahedra strain increase in value with increasing pressure.

It has been shown that the relative compressibilities of the polyhedral cation sites in the perovskite structure give an indication as to how the octahedra rotate upon compression, either by increase in rotation, tending towards lower symmetry, or a reduction in rotation and an increase in symmetry. A model based upon the bond valence concept for each polyhedra has been developed that predicts the compressibility of the polyhedra.[39] The value M_i is the total estimated variation of bond valence in a polyhedral site due to the change of average bond distance.[40] The relative values of the values of M_i for the two polyhedra predicts the behaviour upon compression (see ESI†). For $CsCaCl_3$ based upon our current data and reference values elsewhere[41] we derive a M_{Cs}/M_{Ca} ratio of ~0.4 and predict that the $CsCl_{12}$ polyhedra will be more compressible than the $CaCl_6$ octahedra and as a result the structure will become more distorted with increasing pressure as is observed experimentally in the current study. The value of the ratio is significantly lower than that observed for oxide perovskites but may well reflect the difference in
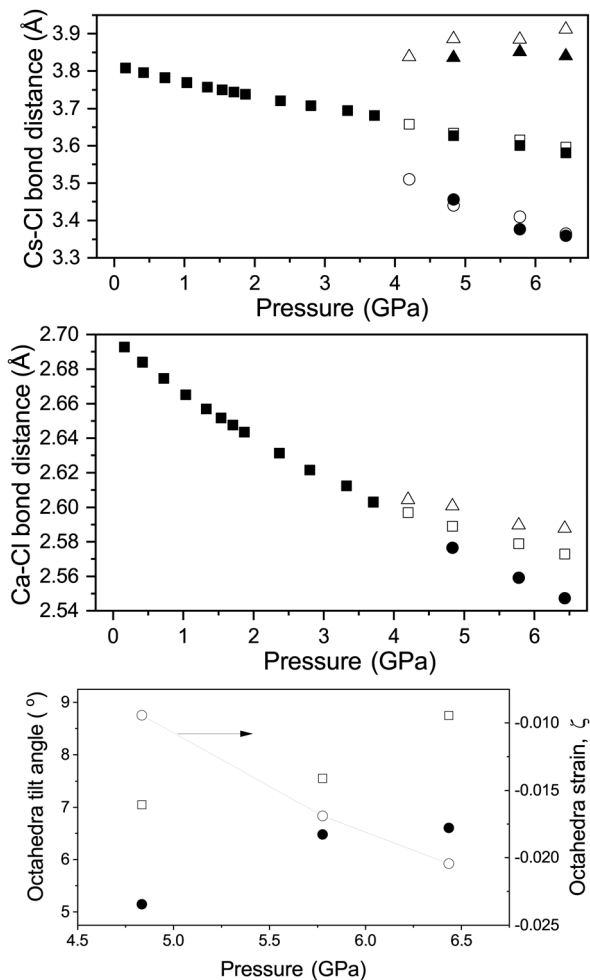

Fig. 9 Top: Variation in Cs–Cl bonds within the $CsCl_n$ polyhedra of $CsCaCl_3$ with increasing pressure. Filled squares represent the the cubic phase. Unfilled circles, squares and triangles the tetragonal phases and the filled circles, squares and triangles the rhombohedral. Middle: Variation in the Ca–Cl bonds in the $CaCl_6$ octahedra with pressure. Filled squares in the cubic phase, unfilled triangles the tetragonal phase and the filled circles in the rhombohedral phase. Bottom: Shows the variation in the octahedra tilts in the tetragonal (ϕ) and rhombohedral (ω) phases with pressure and the variation in octahedra strain (ζ) in the rhombohedral phase (unfilled circles) as defined in the main text.

compressibilties of the oxide and halide polyhedra. Such a low value of the M_i ratio has also been observed for other $1^+:2^+$ halide based materials such as $KCaF_3$ M_K/M_{Ca} ratio of ~0.5 which predicts the structural deformation of $KCaF_3$ should increase with pressure which is also observed experimentally.[42]

3.4 Towards a phase diagram of $CsCaCl_3$

Compression of $CsCaCl_3$ was also performed at 190 K, which permits the determination of tentative phase boundaries for the cubic → tetragonal → rhombohedral phases. Linear extrapolation of the phase boundaries using the two data points for the tetragonal–rhombohedral phase transition suggest that at ambient pressure the rhombohedral phase will not be

4806 | *J. Mater. Chem. C*, 2024, **12**, 4800–4808

This journal is © The Royal Society of Chemistry 2024

observed, even as low as 0 K (where the phase boundary tetragonal to rhombohedral phase is expected to occur at ~ 0.75 GPa) and the Clapeyron slope for the phase boundary is estimated from the two known points as 13 MPa K^{-1}. The phase boundary of the cubic-tetragonal phase appears to be linear from the three data points (one at ambient pressure and two above) and a Clapeyron slope is estimated to have a value of 22 MPa K^{-1}.

4 Conclusion

We have measured by neutron powder diffraction, and heat capacity measurement, the phase behaviour of the perovskite-like material $CsCaCl_3$ as as function of temperature and pressure. Like oxide-based equivalent materials it undergoes a series of phase transitions which show a stepwise change in symmetry. We have derived the bulk modulus at room temperature of the cubic phase and have also determined a tentative phase diagram for the material along with some fundamental thermodynamic properties.

Conflicts of interest

The authors declare no conflicts of interest.

Acknowledgements

Notes and references

1 J. Fernández, M. Tello and M. Arriandiaga, *Mater. Res. Bull.*, 1978, **13**, 477–490.

2 V. M. Goldschmidt, *Naturwissenschaften*, 1926, **14**, 477–485.

3 W. Travis, E. N. K. Glover, H. Bronstein, D. O. Scanlon and R. G. Palgrave, *Chem. Sci.*, 2016, **7**, 4548–4556.

4 K. S. Alexandrov, B. V. Besnosikov and L. A. Posdnjakova, *Ferroelectrics*, 1976, **12**, 197–198.

5 Y. Fujii, S. Hoshino, Y. Yamada and G. Shirane, *Phys. Rev. B: Condens. Matter Mater. Phys.*, 1974, **9**, 4549–4559.

6 Y. Shi, Y. Zhou, Z. Ma, G. Xiao, K. Wang and B. Zou, *J. Mater. Chem. C*, 2020, **8**, 12755–12767.

7 F. Aguado, F. Rodriguez1 and A. R. Lennie, *J. Alloys Compd.*, 2012, **541**, 210–214.

8 L. Zhang, L. Wang, K. Wang and B. Zou, *J. Phys. Chem. C*, 2018, **122**, 15220–15225.

9 Y. Vaills, J. Buzaré, A. Gibaud and C. Launay, *Solid State Commun.*, 1986, **60**, 139–141.

10 M. Tyagi, M. Zhuravleva and C. L. Melcher, *J. Appl. Phys.*, 2013, **113**, 203504.

11 C. L. Melcher, *Nucl. Instrum. Methods Phys. Res. A*, 2005, **537**, 6–14.

12 N. Yedukondalu, K. R. Babu, D. J. Bheemalingam, C. Singh, G. Vaitheeswaran and V. Kanchana, *Phys. Rev. B: Condens. Matter Mater. Phys.*, 2011, **83**, 165117.

13 S. Zou, Y. Liu, J. Li, C. Liu, R. Feng, F. Jiang, Y. Li, J. Song, H. Zeng and M. Hong, *J. Am. Chem. Soc.*, 2017, **139**, 11443.

14 E.-P. Yao, Z. Yang, L. Meng, P. Sun, S. Dong, Y. Yang and Y. Yang, *Adv. Mater.*, 2017, **29**, 1606859.

15 L. Lv, Y. Xu, H. Fang, W. Luo, F. Xu, L. Liu, B. Wang, X. Zhang, D. Yang and W. Hu, *Nanoscale*, 2016, **8**, 13589.

16 Q. Wang, X. Zhang, Z. Jin, J. Zhang, Z. Gao, Y. Li and S. F. Liu, *ACS Energy Lett.*, 2017, **2**, 1479.

17 C. L. Bull, N. P. Funnell, M. G. Tucker, S. Hull, D. J. Francis and W. G. Marshall, *High Press. Res.*, 2016, **36**, 493–511.

18 A. D. Fortes, RAL Technical Reports, 2019, RAL-TR-2019-002, year.

19 S. Klotz, J. C. Chervin, P. Munsch and G. L. Marchand, *J. Phys. D: Appl. Phys.*, 2009, **42**, 075413.

20 J. M. Besson, R. J. Nelmes, G. Hamel, J. S. Loveday, G. Weill and S. Hull, *Phys. B*, 1992, **180**, 907–910.

21 O. Arnold, J. C. Bilheux, J. M. Borreguero, A. Buts, S. I. Campbell, L. Chapon, M. Doucet, N. Draper, R. Ferraz Leal, M. A. Gigg, V. E. Lynch, A. Markvardsen, D. J. Mikkelson, R. L. Mikkelson, R. Miller, K. Palmen, P. Parker, G. Passos, T. G. Perring, P. F. Peterson, S. Ren, M. A. Reuter, A. T. Savici, J. W. Taylor, R. J. Taylor, R. Tolchenov, W. Zhou and J. Zikovsky, *Nucl. Instrum. Meth. A*, 2014, **764**, 156–166.

22 B. H. Toby, *J. Appl. Crystallogr.*, 2001, **34**, 210–213.

23 M. J. Cliffe and A. L. Goodwin, *J. Appl. Crystallogr.*, 2012, **45**, 1321–1329.

24 A. M. Glazer, *Acta Crystallogr., Sect. B: Struct. Sci.*, 1972, **28**, 3384–3392.

25 K. S. Knight, W. G. Marshall and P. M. Hawkins, *Phys. Chem. Miner.*, 2014, **41**, 461–472.

26 K. S. Knight, *J. Solid State Chem.*, 2018, **263**, 172–181.

27 K. S. Knight, *J. Mater. Sci.*, 2020, **55**, 6417–6428.

28 D. C. Wallace and H. Callen, *Am. J. Phys.*, 1972, **40**, 1718–1719.

29 K. Knight, *J. Mater. Sci.*, 2020, **55**, 6417–6428.

30 Z. Liu, Y. Pan, X. Fu, Y. Ding and L. Li, *J. Mater. Chem. C*, 2024, DOI: **10.1039/D3TC04189A**.

31 M. A. Rahman, F. Mostari, M. Z. Hasan, A. Irfan, M. F. Rahman, M. J. Hosain, S. C. Mouna, I. A. Chowdhury, M. Rasheduzzaman and M. Choudhury, *Phys. B*, 2023, **669**, 415260.

32 G. J. Fischer, Z. Wang and S.-I. Karato, *Phys. Chem. Miner.*, 1993, **20**, 97.

33 A. Verma and A. Kumar, *J. Alloys Compd.*, 2012, **541**, 210–214.

34 M. Lal and S. Kapila, *Int. J. Mater. Sci.*, 2017, **12**, 137–147.

35 V. Monteseguro, D. Errandonea, S. N. Achary, J. A. Sans, F. J. Manjón, S. Gallego-Parra and C. Popescu, *Inorg. Chem.*, 2019, **58**, 10665–10670.

36 C. L. Bull and K. S. Knight, *Solid State Sci.*, 2016, **57**, 38–43.

37 H. D. Megaw and C. N. W. Darlington, *Acta Crystallogr., Sect. A: Found. Crystallogr.*, 1975, **31**, 161–173.

This journal is © The Royal Society of Chemistry 2024

J. Mater. Chem. C, 2024, **12**, 4800–4808 | **4807**

38 M. A. Carpenter, E. K. Salje and A. Graeme-Barber, *Eur. J. Mineral.*, 1998, **10**, 621–691.

39 J. Zhao, N. L. Ross and R. J. Angel, *Acta Crystallogr., Sect. B: Struct. Sci.*, 2004, **60**, 263–271.

40 I. D. Brown and D. Altermatt, *Acta Crystallogr., Sect. B: Struct. Sci.*, 1985, **41**, 244–247.

41 N. E. Brese and M. O'Keeffe, *Acta Crystallogr., Sect. B: Struct. Sci.*, 1991, **47**, 192–197.

42 K. S. Knight, *J. Alloys Compd.*, 2017, **693**, 1305–1314.

43 C. L. Bull, C. J. Ridley and N. P. Funnell, Compression Behaviour of Tetragonal CsCaCl₃, STFC ISIS Neutron and Muon Source, 2020, vol. 14, DOI: **10.5286/ISIS.E.RB2010752**.

4808 | *J. Mater. Chem. C*, 2024, **12**, 4800–4808

This journal is © The Royal Society of Chemistry 2024